Plant-Based Shape Memory Cryogel for Hemorrhage Control

J. Deng, Z. Zhao, X.Y. Yeo, C. Yang, J. Yang, A.R. Ferhan, B. Jin, C. Oh, S. Jung,* S. Suresh,* and N.-J. Cho*

The escalating global demand for sustainable manufacturing, motivated by concerns over energy conservation and carbon footprints, encounters challenges due to insufficient renewable materials and arduous fabrication procedures to fulfill specific requirements in medical and healthcare systems. Here, biosafe pollen cryogel is engineered as effective hemostats without additional harmful crosslinkers to treat deep noncompressible wounds. A straightforward and low-energy approach is involved in forming stable macroporous cryogel, benefiting from the unique micro-hierarchical structures and chemical components of non-allergenic plant pollen. It is demonstrated that the pollen cryogel exhibits rapid water/blood-triggered shape-memory properties within 2 s. Owing to their inherent nano/micro hierarchical structure and abundant chemical functional groups on the pollen surface, the pollen cryogel shows effective hemostatic performance in a mouse liver penetration model, which is easily removed after usage. Overall, the self-crosslinking pollen cryogel in this work pioneers a framework of potential clinical applications for the first-hand treatment on deep noncompressible wounds.

1. Introduction

The timely control of bleeding in civilian accidents and military battlefields is essential to prevent excessive blood loss, which can lead to high mortality rates from penetrating wounds or deep trauma.[1,2] While conventional hemostats in the form of cotton gauzes,[3] collagen-based sponges,[4,5] and fibrin-based bandages,[6] are known to be capable of managing external hemorrhage, there is a critical need to develop robust hemostats providing swift control of hemorrhage from irregularly shaped, deep, and noncompressible wounds prehospital.[7]

Shape-memory foams and sponges show great promise as hemostats because of their ability to be easily compressed and highly durable, making them suitable for filling deep noncompressible wounds.[8] Additionally, commercially available miniature cellulose sponges can be directly applied to wound cavities, expediting hemostatic actions.[9]

Despite their advantages, these materials also have certain limitations. For example, polymer foams derived from substances like polyurethane[10,11] and thiol-epoxy[12] have limited absorption capabilities and expand relatively slowly, which makes them less ideal for swift hemostatic use.[11,13] On the other hand, although commercial miniature cellulose sponges are user-friendly, their blood absorption is constrained due to the absence of extensive interconnected porous

J. Deng, C. Yang, J. Yang, A. Ferhan, N.-J. Cho
School of Materials Science and Engineering
Nanyang Technological University
50 Nanyang Avenue, Singapore 639798, Singapore
E-mail: njcho@ntu.edu.sg

J. Deng, A. Ferhan, N.-J. Cho
Centre for Cross Economy
Nanyang Technological University
50 Nanyang Avenue, Singapore 639798, Singapore

Z. Zhao
Hubei Key Laboratory of Biomass Resource Chemistry and Environmental Biotechnology
Hubei International Scientific and Technological Cooperation Base of Sustainable Resource and Energy
Hubei Engineering Center of Natural Polymers-based Medical Materials
School of Resource and Environmental Science
Wuhan University
Wuhan 430079, China

X. Yeo, B. Jin, C. Oh, S. Jung
Department of Medical Science
College of Medicine
CHA University
Gyeonggi-do 13488, Republic of Korea
E-mail: jungsy0505@cha.ac.kr

S. Suresh
Department of Materials Science and Engineering
Massachusetts Institute of Technology
Cambridge, MA 02139, USA
E-mail: ssuresh@mit.edu

networks.[7] Furthermore, using them often necessitates invasive procedures for the removal of each mini-sponge after use.[14]

In this regard, cryogels have emerged as potentially superior hemostats over shape memory foams and sponges owing to a more highly interconnected network of macropores that facilitate greater and quicker blood absorption, especially from deep internal wounds.[15,16] The form and size of the pollen cryogels can be tailored through mold casting, enabling a range of shapes and sizes to fit different wounds.

Cryogels are traditionally produced following a lyophilization process,[17] which is time-consuming, energy-intensive,[18] and mainly involves synthetic polymers derived from nonrenewable petrochemicals.[19] In addition, there are stringent requirements for consistency, quality, and safety that need to be fulfilled for medical applications, all of which entail an additional set of energy-intensive processes.[20] With growing global demand to minimize carbon footprint, there is increasing emphasis in the biomedical industry to develop fabrication approaches that are more environmentally sustainable.[21] In the context of cryogel fabrication, this can be addressed by the solvent-exchange method, which uses water-miscible solvents instead of vacuum to remove ice crystals. This obviates the need to use energy-intensive equipment and is regarded as an environmentally sustainable alternative to conventional lyophilization.[15,22–24]

Natural biopolymers such as cellulose, collagen, and gelatin have been used to fabricate cryogels by recourse to the solvent-exchange method.[4,5,25–30] However, following the extraction and refining of these biopolymers from raw biomass,[31] the addition of crosslinkers, such as sodium metaperiodate,[32] heavy metal ions,[29] and carbon nanotubes,[14,33] are necessary to strengthen the structural integrity of cryogels to withstand mechanical stresses imposed by dissolving ice crystals (Table S1, Supporting Information).[28,34,35] Unfortunately, such crosslinkers can be detrimental to human health, thereby severely restricting their use in biomedical applications.[36,37] Such limitations highlight the need to develop new classes of mechanically robust and biologically safe cryogels that can be fabricated more efficiently and sustainably from renewable natural materials. Pollen, which is an abundant natural resource with unique properties such as a hollow internal architecture, uniform microscale size, and robust hierarchical structure,[38–42] has recently been the focus of the development of novel classes of eco-friendly derivative materials. Our previous work has shown that raw pollen grains could be converted into soft nonallergenic granular pollen microgels through an alkaline treatment, akin to soap-making, which is more facile and energy-saving than the extraction of biopolymers from macroscopic raw biomass.[39,43–45]

Motivated and guided by our previous findings[39,43–46] on the unique properties of pollen as a sustainable material for different engineering and biomedical applications, we develop in this work pollen-based shape-memory cryogels. This unique approach entails a compression-driven self-crosslinking process without the addition of chemical crosslinkers. This process is enabled by the hollow microsphere structures and components of the granular pollen microgels. Since they exhibit excellent hemocompatibility and biocompatibility, the pollen cryogels offer promising new pathways for treating noncompressible deep hemorrhages.

2. Results and Discussion

Macroporous pollen cryogels were prepared using natural raw sunflower bee pollen (*Helianthus annuus*) through self-crosslinking. They exhibit excellent shape-memory properties that make them suitable for treating deep non-compressible wounds (**Figure 1**). Sunflower pollen grains, abundant in nature and harvested by bees, have distinctive core-shell structures with spiky architectures.[39] Their shells comprise two layers, an ultra-strong sporopollenin outer layer and a flexible inner layer consisting of cellulose and pectin.[41,47] The raw pollen grains were first transformed into pollen microgels via defatting and alkaline incubation.[39] Subsequently, the pollen microgels were processed into pollen cryogels through a stepwise compression-driven self-crosslinking approach, avoiding the use of an energy-intensive lyophilizer. The resulting pollen cryogels were then immersed in deionized (DI) water to obtain hydrated cryogels for further characterization (Figure S1a,b, Supporting Information). Pollen cryogels were produced in various quantities, ranging in size from several millimeters to several centimeters, which demonstrated that the self-crosslinking method was capable of meeting industrial requirements for ease of processing and scale-up (Figure S1c, Supporting Information).

It is essential for the pollen cryogels to possess structural stability and mechanical robustness in biofluid environments to be effective in treating deep noncompressible hemorrhage (**Figure 2**). To test the mechanical properties of the pollen cryogels in a hydrated state, uniaxial compression tests were conducted. We first investigated the influence of the water content of the initial pollen microgel suspensions on the mechanical properties of pollen cryogels. We found that the viscosity of pollen microgels increased with a decrease in water content from 98.7% to 96.7%, while the 96.7% water content of pollen microgel suspension is with too high viscosity to squeeze into the mold easily (Figure S2, Supporting Information). Besides, Young's modulus of the cryogels increased from 5 kPa to around 10 kPa with a decrease in water content from 98.7% to 97.4% (Figure 2a; Figure S3, Supporting Information). Furthermore, the density of cryogels increased with a decrease in water content (Table S2, Supporting Information). Based on these observations, pollen microgels with a water content of ≈97.4% were selected for subsequent experiments.

Our earlier work has established that a longer incubation period of the pollen microgel suspension in an alkaline solution would lead to a more extensive de-esterification of the pollen particles, which have the potential to impact the mechanical properties of pollen cryogels.[39,44,45] Therefore, we compared Young's modulus in compression of hydrated cryogels fabricated from pollen microgels under a range of incubation periods of 0, 12, 24, 36, and 48 h, respectively (Figure 2b; Figure S4, Supporting Information). It was demonstrated that 0 h incubated pollen cryogels had the highest Young's modulus of ≈20 kPa. With prolonged incubation time, Young's modulus decreased and stabilized at around 10 kPa. However, compared to samples subjected to longer incubation time, the stress-strain curve of the 0 h incubated sample displayed pronounced hysteresis, indicating high energy dissipation (Figure S4, Supporting Information), which was unsuitable for rapid shape recovery. Among 0, 12, 24, 36, and 48 h incubated pollen cryogels, the 24 h incubated sample exhibited the highest Young's modulus (Figure 2b).
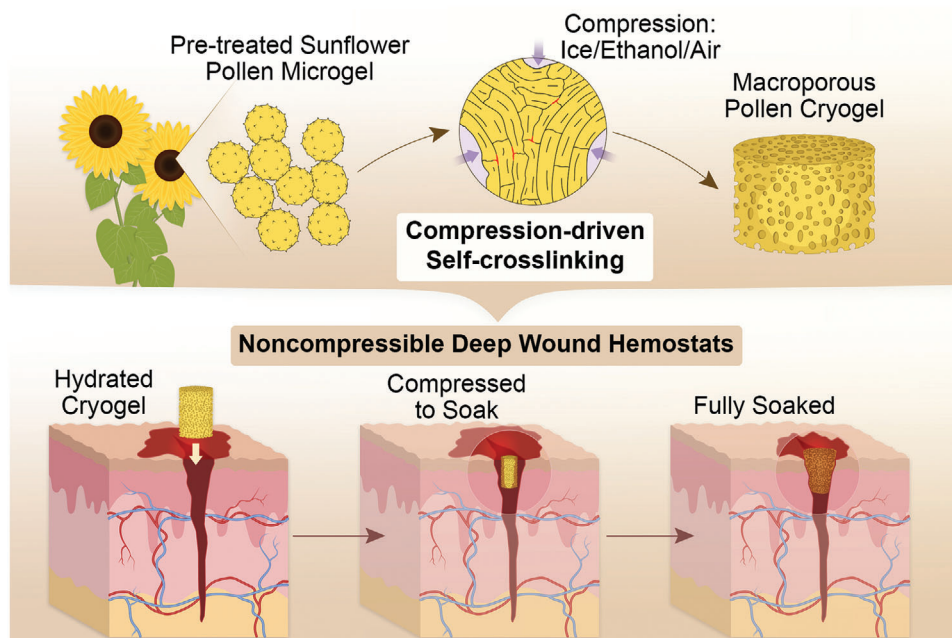
ADVANCED
SCIENCE NEWS
www.advancedsciencenews.com

ADVANCED
MATERIALS
www.advmat.de

Figure 1. Schematic representation of pollen cryogels. Schematic showing the fabrication of pollen cryogels using compression-driven self-crosslinking and representation of their application as hemostats for treating noncompressible deep wounds.
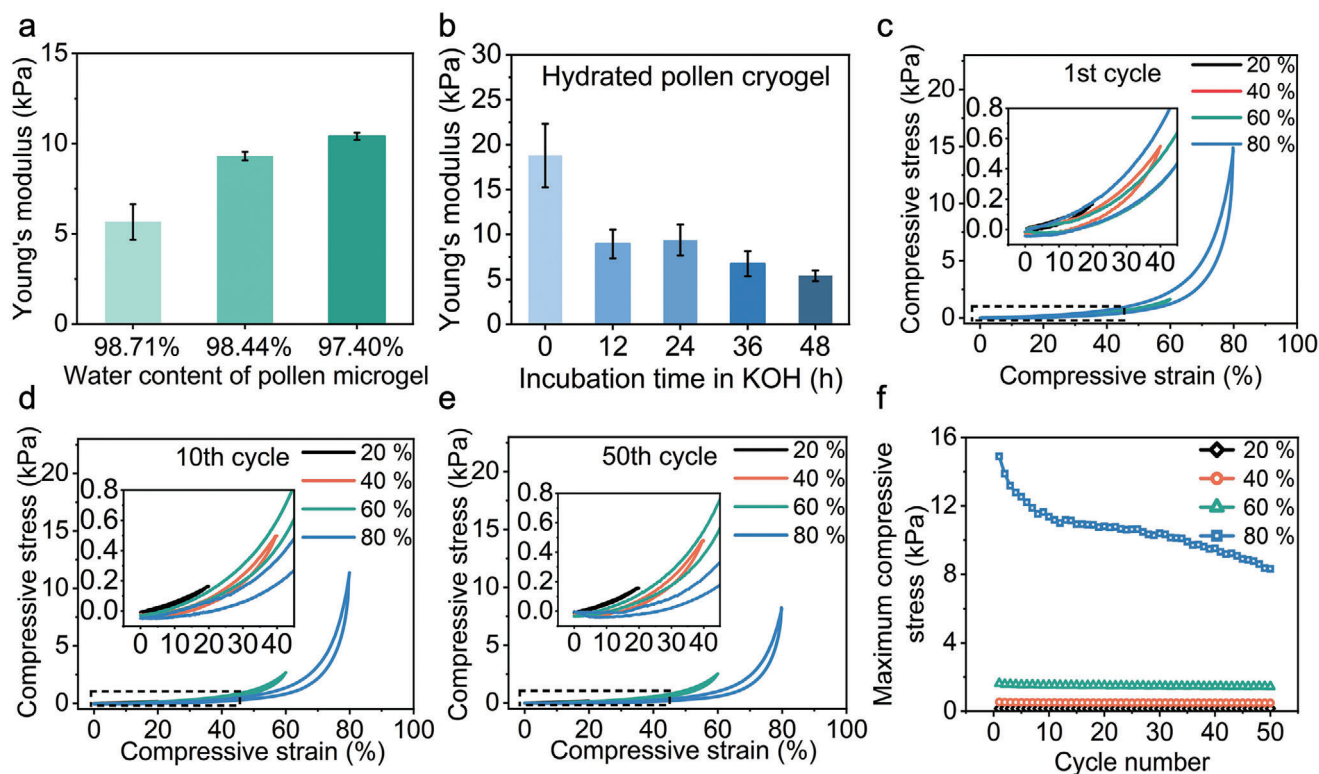

Figure 2. Mechanical properties of pollen cryogels in a hydrated state. a) Comparison of Young's modulus of hydrated pollen cryogels fabricated from pollen microgels with different water contents. b) Young's modulus of hydrated pollen cryogels for different incubation times. Stress–strain curves of pollen cryogels with repeated (cyclic) compression at 20%, 40%, 60%, and 80% uniaxial compressive strains at the c) first, d) tenth, and e) fiftieth cycles. f) The variation of maximum compressive stress with the number of compressive cycles.

We then examined the mechanical rigidity of the hydrated pollen cryogels after 1, 10, and 50 cycles of compression loading to different levels of compressive strain (Figure 2c–e). In all the dynamic compression tests, the pollen cryogels presented negligible loss of strain recovery after unloading and no observable structural failure under 20%, 40%, and 60% of compressive strain. However, a significant loss of strain recovery after unloading was observed when the cryogels were cyclically compressed under 80% of strain for 50 cycles. In addition, the maximum compressive stress was reduced from 15 to 8 kPa under 80% of compressive strain (Figure 2f). Besides, we also compared the area change of the hysteresis loop as a function of compression cycles under 20%, 40%, 60%, and 80% of compressive strain (Figure S5, Supporting Information). It is found that the areas of hysteresis loops decreased with the increase in cycle times, which indicated the cyclic softening, that the cyclic compression loading eliminated the initial difference of the mechanical properties due to prestrain and made the mechanical properties of materials tend to be uniform.

Moreover, the pollen cryogels in phosphate-buffered saline (PBS) solution showed no discernible loss of strain recovery when they were compressed to 20%, 40%, 60%, and 80% strain (Figures S6 and S7, Supporting Information). The salts in PBS solution, including sodium (Na^+) and potassium ions (K^+), decreased the repulsive electrostatic forces between carboxyl groups (COO^-) in pollen cryogels, which compacted the structures of pollen cryogels, dehydrated the wet cryogels, and improved the mechanical properties. Overall, the pollen cryogels exhibited good hydro-stability and compression strain recovery properties.

To understand the structural changes behind the formation of pollen cryogels, we analyzed the morphological properties and molecular structure of the pollen specimens at different stages during the transformation from pollen microgel to cryogel (**Figure 3**; Figure S8, Supporting Information). During this process, the pollen microgel was first frozen at −20 °C for 12 h. It was then subjected to a 48 h solvent-exchange process to obtain ethanol-exchanged pollen microgel and finally ambient-dried for 24 h to obtain the pollen cryogel (Figure 3a). A series of Field-Emission Scanning Electron Microscope (FESEM) images revealed clear morphological changes at the mesoscale across the as-prepared pollen microgel, frozen pollen microgel, ethanol-exchanged pollen microgel, and cryogel samples (Figure 3b). As-prepared pollen microgels consist of discrete granular particles with intrinsic spiky and hollow morphologies. In contrast, the individual pollen particles were indiscernible in the frozen microgel and a porous structure was instead observed with lamellar pore walls comprising overlapping plates. After ethanol immersion, the overall porous structure remained intact. However, there was a difference in the pore morphology with the pores appearing more elongated. The pore wall also appeared to be more compact. Further subtle changes in pore morphology were observed in the cryogel. In this final state, the pore wall appeared highly densified with smaller pores.

To determine whether the observed structural changes were facilitated by chemical interactions, we extended our investigation using potassium bromide-Fourier Transform Infrared (KBr-FTIR) spectroscopy (Figure 3b). The absorbance peak within the range of 3395–3370 cm^{-1} is assigned to the O–H stretching vibration of hydroxyl groups (vOH), and the absorbance peak between 1104 to 1060 cm^{-1} is assigned to the C–O stretching vibration of carboxyl groups.[48–51] The O–H stretching vibration peak shifted from 3391 cm^{-1} to 3387 cm^{-1} after the pollen microgels were frozen. This peak further shifted to 3383 cm^{-1} after ethanol exchange and finally reached 3272 cm^{-1} in the final state of pollen cryogel. These redshifts of the stretching resonance bands of O-H groups and the broadening of the peaks in forming pollen cryogels can be ascribed to the establishment of new hydrogen bonds during the formation of pollen cryogel.[52,53] In addition, the C–O stretching vibration peak also shifted from 1104 cm^{-1} to 1057 cm^{-1}, pointing to an increasing number of hydrogen bonds during the formation of pollen cryogels.[54]

Based on the visual evidence from FESEM and FTIR analysis, we deduce that the formation of pollen cryogels follows the mechanism illustrated in Figure 3d. Prior to freezing, the hollow granular pollen particles crowded together randomly in the pollen microgel solution owing to low water content.[55] Upon freezing at −20 °C, the formation of ice crystals forces adjacent pollen particles to organize into a close-packed arrangement. The continuous growth of the ice crystals exerting pressure on the surrounding particles results in the flattening and stacking of the pollen particles. Their granular hollow shapes remained intact in the presence of sporopollenin,[56] and effectively transferred the compression forces across one another, facilitating surface contact and more hydrogen bonds. The hierarchical spiky surface morphology of sunflower pollen particles could also contribute to bonding due to the physical mesh assembly between the neighbor spikes.[40] When the frozen pollen microgels were immersed in ethanol for dehydration, the ice crystals dissolved and were replaced by ethanol to retain stable macroporous structures. This dehydration process forced pollen microgel particles to bind more tightly, thereby strengthening the hydrogen bonds to enable them to withstand the thawing force from the dissolution of ice crystals.[57] Subsequently, the samples, fully immersed in ethanol, were dried under ambient conditions,[58] with pollen particles forming more dense pore walls of the final pollen cryogels, as seen in the FESEM images and KBr-FTIR results. Additionally, we also compared the structures of water and ethanol-exchanged frozen pollen microgels (Figure S9, Supporting Information). The water-exchanged cylindrical frozen microgel melted quickly at room temperature, exhibiting gradual fragmentation with prolonged immersion time in the water bath, and ultimately broke into small pieces within 30 min. In contrast, the ethanol-exchanged frozen pollen microgel maintained an intact and porous structure and shrank slightly over 30 min, which indicated that dehydration in ethanol is indispensable to forming stable pollen cryogels during the solvent-exchange process.

We also assessed the in vitro water/blood (anticoagulated mouse blood) absorption abilities of the pollen cryogels fabricated under various KOH (10 wt%) incubation periods; anticoagulated mouse blood has commonly been used for the hemostat evaluation.[14,59] The swelling ratio in DI water of cryogels prepared under different KOH incubation times was identical, at around 2600% (Figure S10, Supporting Information). However, we observed differences in their absorption capacity with the cryogel prepared under 24 h incubation in KOH showing the highest capacity, reaching nearly 4 g cm^{-2} at steady-state (**Figure 4**a). It also produced the quickest absorption with an initial rate (i.e., within the first two seconds) of ≈2 g cm^{-3} s^{-1}
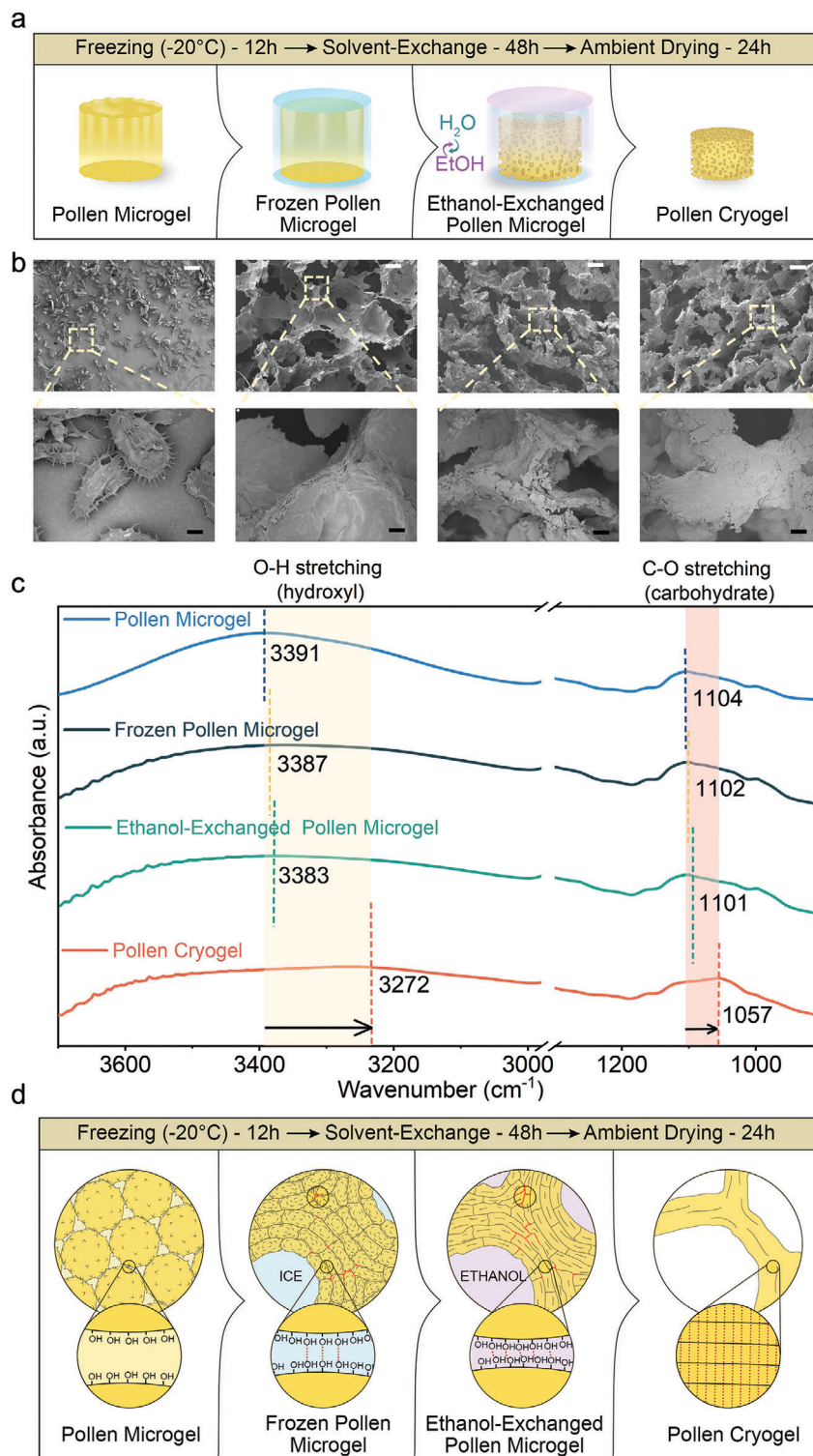
Figure 3. Fabrication method and characterization for pollen cryogels. a) The fabrication process and four states of samples during the formation of pollen cryogels, including granular pollen microgels, frozen pollen microgels, ethanol-exchanged pollen microgels, and macroporous pollen cryogels. b) Field-emission scanning electron microscope (FESEM) images of samples from four different states at different magnifications. The white scale bars represent 100 µm, and the black bars represent 10 µm. c) Potassium bromide-Fourier Transform Infrared (KBr-FTIR) spectra of samples for the four different states. d) Schematic mechanism of the compression-driven self-crosslinking method to fabricate pollen cryogels from granular pollen microgel.
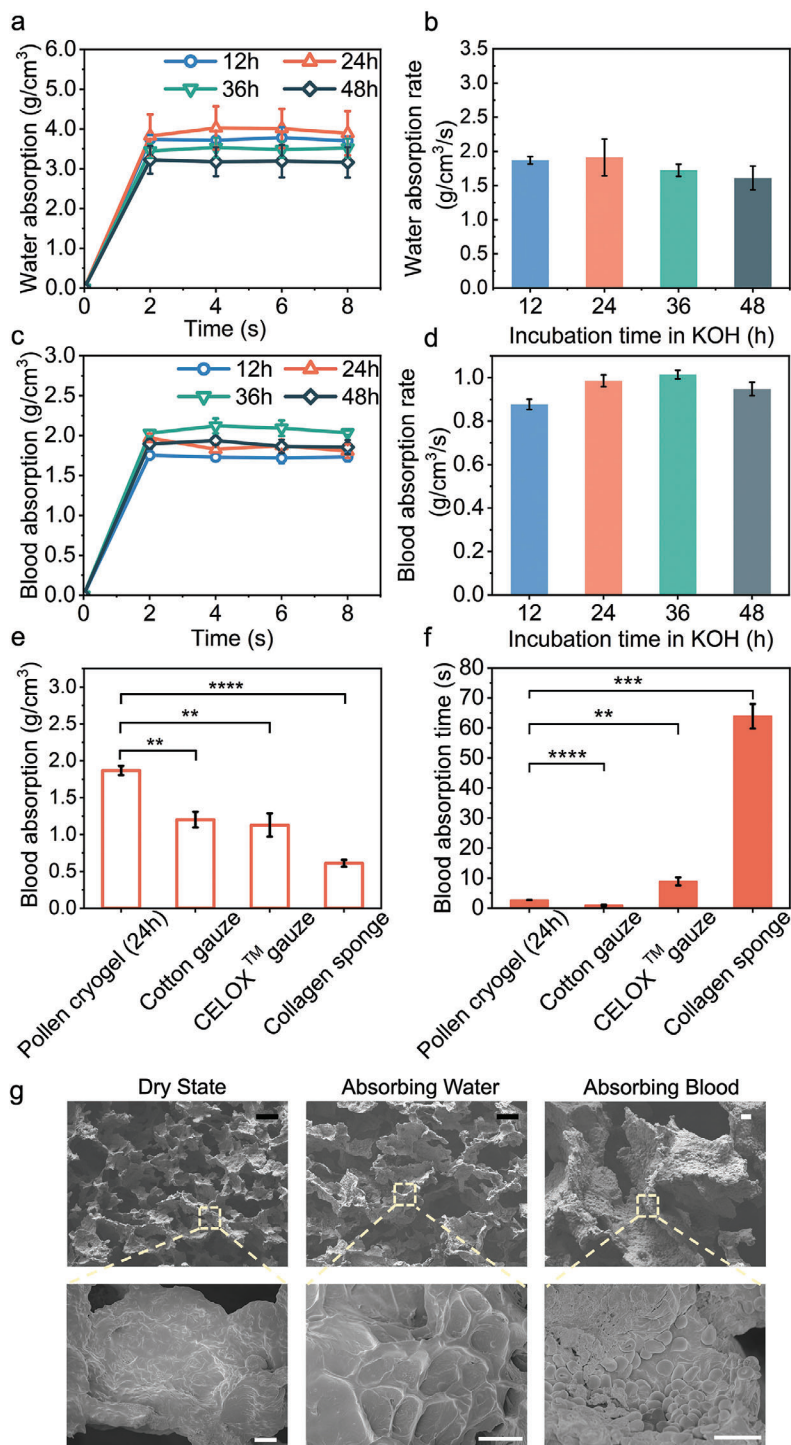
Figure 4. In vitro water and blood (anticoagulated mouse blood) absorption properties of pollen cryogels fabricated by self-crosslinking method: a) Water absorption capacity-time dynamic curves. b) Water absorption rate of pollen cryogels as a function of different incubation times. c) Blood absorption capacity-time dynamic curves. d) Blood absorption rate of pollen cryogels as a function of different incubation times. Comparison of e) blood absorption capacity and f) blood absorption time between pollen cryogels and other commercially available products, i.e., cotton gauze, CELOX gauze, and collagen sponge. g) FESEM images showing the micro/nano hierarchical structure of as-prepared pollen cryogels, the cryogels before and after absorbing water and blood. The black scale bars represent 100 μm, and the white scale bars represent 10 μm. The statistical significance of the observed trends was calculated using Student's t-test (two-sided). $*p < 0.05$, $**p < 0.01$, $***p < 0.001$, $****p < 0.0001$, $n = 3$.

**ADVANCED
SCIENCE NEWS**

www.advancedsciencenews.com

**ADVANCED
MATERIALS**

www.advmat.de

(Figure 4b). When absorbing blood, the pollen cryogels always presented stable maximum blood absorption capacity, ranging from 1.75 to 2 g cm^{-2} (Figure 4c), and the 24 and 36 h incubated pollen cryogels displayed the most rapid blood absorption, with an initial rate of ≈1 to 1.1 g cm^{-3} s^{-1} (Figure 4d). This strong fluid absorbability of pollen cryogels was attributed to the interconnected structures and macroporous architectures with pore sizes ranging from 100 to 200 μm, as shown in cross-sectional FESEM images in Figure 3. Considering their favorable water/blood absorption ability and good mechanical properties, the pollen cryogels fabricated from 24 h alkaline incubation time are identified to be the best choice for use as hemostats.

We then compared the blood absorption properties of our pollen cryogel (24 h incubation) and other commercial products, including cotton gauze, CELOX gauze, and collagen sponge. Further details of the commercial products are provided in Table S3 (Supporting Information). Among the tested samples, the pollen cryogel exhibited the highest blood absorption capacity of around 1.8 cm^3 g^{-1}, superior to other commercial products, which exhibited absorption capacities lower than 1.25 cm^3 g^{-1} (Figure 4e) (p < 0.01). Furthermore, we introduced a 500 μL droplet of blood (anticoagulated mouse blood) on the commercial products and our prehydrated pollen cryogel to measure absorption time. Our hydrated pollen cryogel (24 h incubation) absorbed blood after 2.7 ± 0.1 s, which was more than three times faster than blood absorption by CELOX-gauze and collagen sponge, at 8.9 ± 1.1 s (p < 0.01) and 63.9 ± 5.1 s (p < 0.001), respectively (Figure 4f). The macroscopic structural morphology of the pollen cryogel was observed by FESEM in the dry state, the states after absorbing water and blood (Figure 4g). Notably, the nano-scale spikes and microscale undulated structures, from the special morphology of sunflower pollen particles, were observed on the surface of pore walls following water absorption. Generally, the desirable fluid penetration speed can be attributed to the highly interconnected open macropores of the prehydrated pollen cryogel. The high surface roughness of pore wall structures is also one of the main parameters enhancing the efficacy of blood hemostats.[60]

The shape-memory characteristics of pollen cryogels are of paramount importance in their application as hemostatic agents for addressing deep noncompressible hemorrhage, as they enable rapid volume expansion, facilitate precise delivery into confined wounds, and ensure thorough coverage of irregular wound boundaries. We compared the shape-memory properties of pollen cryogels fabricated following different KOH (10 wt%) incubation time. The pre-hydrated pollen cryogels were uniaxially compressed and then subjected to the absorption of blood and water to probe the recovery ratio based on the uniaxial height change. The pollen cryogels prepared following 12, 24, and 36 h KOH incubation achieved an almost 100% height recovery in water (**Figure 5a**), taking nearly 1.25 s to complete the recovery process (Figure 5b). In comparison, pollen cryogels prepared following 48 h KOH incubation achieved only 70% height recovery over 1.2 s. The shape recovery ratio of the pollen cryogels remained relatively consistent when triggered by blood, around 95% of the height recovery ratio, regardless of different KOH incubation periods (Figure 5c). The pollen cryogels required a longer height recovery time when absorbing blood compared to water, which can be attributed to the higher viscosity of blood[4,30] (Figure 5d; Figure S11, Supporting Information). Overall, the

shape recovery rate of the pollen cryogels was much faster than that of other shape memory hemostatic agents. For example, XStat required 25 seconds to recover shape in blood, Quaternized chitosan/Polydopamine (QCS/PDA) required around 40 seconds in blood, and microchannelled alkylated chitosan sponge (MACS) required 2.5 seconds in blood,[26,59] as shown in Table S4 (Supporting Information). Although most of the shape-memory hemostats have highly crosslinked pores, they recover the shapes owning to the penetration of blood. Our pollen cryogels not only have macropores for blood absorption, the unique overlapped granular particles also offer nanopores to absorb blood fluids for rapid shape recovery. Furthermore, we assessed the height recovery stability of the pollen cryogels by performing cyclic absorption/desorption experiments while immersing them in mouse blood (Figure S12a, Supporting Information). To emulate biomedical applications, pollen cryogels were first immersed in PBS solution. The desorption and reabsorption processes were repeated over ten cycles, and the height changes were recorded. The pollen cryogels recovered almost entirely in the first three cycles and maintained a high recovery ratio of roughly 90% by the tenth cycle (Figure S12b, Supporting Information). The height recovery ratio observed in cyclic tests points to the structural stability of the pollen cryogels. This characteristic helps to impart sustained full-volume expansion under conditions of recurrent compression, a pivotal attribute for the efficacious treatment of deep noncompressible wounds in clinical settings.

The capability of pollen cryogels to function as coagulant contributes to one of their appealing characteristics as hemostats. This capability is typically evaluated by performing dynamic whole-blood-clotting tests, which involve measuring the absorbance value of the hemoglobin solution, known as the blood clotting index (BCI).[59,61] A lower BCI value indicates a higher blood clotting rate and a greater pro-coagulant ability. The BCI of pollen cryogels was compared to that of several commercial products, namely collagen sponge, cotton gauze, and CELOX gauze, where the pollen cryogels had significantly lower BCI values than the collagen sponge and cotton gauze but had a BCI value comparable to that of CELOX gauze (**Figure 6a**).

The aggregation of RBCs and adhesion of platelets were strongly related to the active coagulation cascade. To further investigate the hemostatic properties of pollen cryogels, the aggregation and surface adhesion characteristics of red blood cells (RBCs) and platelets in mouse blood were observed in comparison with three control groups, cotton gauze, CELOX gauze, and collagen sponge (Figure 6c). FESEM characterization revealed that a large number of RBCs and platelets adhered to pollen cryogels, as well as CELOX gauze and collagen sponge (Figure 6b). The results appear to suggest that the interconnected macropores within the pollen cryogels mainly contributed to blood penetration and adhesion of RBCs and platelets, and the inherent surface bump and spikes inside pollen cryogels further promoted active capture and aggregation.

We then evaluated the hemocompatibility of the pollen cryogels by performing an in vitro hemolysis assay to estimate their suitability for use in biomedical applications.[62] Pollen cryogels were ground into powder and dispersed in a PBS solution to concentrations of 0, 625, 1250, 2500, and 5000 μg mL^{-1}. The centrifugally obtained supernatants from pollen cryogels, blank negative group (PBS solution), and positive Triton X-100 group were

**ADVANCED
SCIENCE NEWS**

www.advancedsciencenews.com
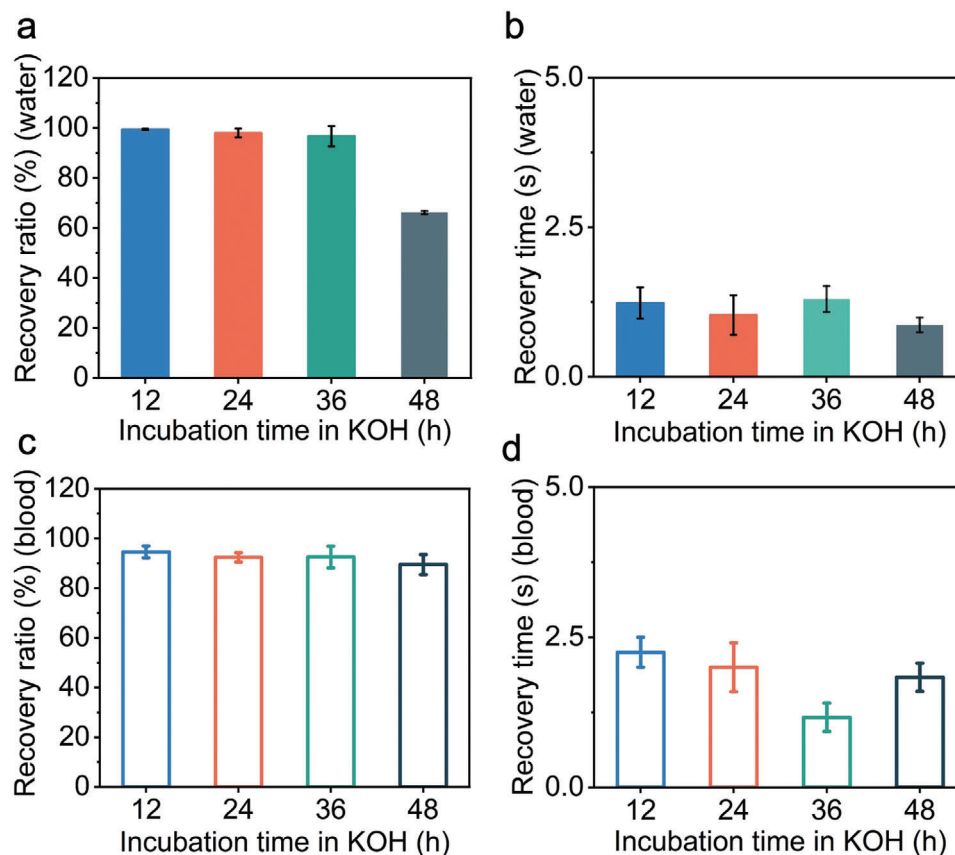
**ADVANCED
MATERIALS**

www.advmat.de

Figure 5. Shape-memory property of pollen cryogels fabricated by the self-crosslinking method: a) Shape-recovery ratio in height and b) Shape-recovery time of uniaxially compressed hydrated cryogels that were prepared following different incubation time in KOH, after reabsorbing water. c) Shape-recovery ratio in height and d) Shape-recovery time of uniaxially compressed hydrated cryogels that were prepared following different incubation time in KOH, after absorbing blood (anticoagulated mouse blood).

observed, and the hemolysis ratio was tested. It is shown that all the concentrations of pollen cryogel groups presented a light yellow color similar to the blank negative group, while the Triton X-100 (positive group) showed a bright red color owing to the hemolysis phenomenon (Figure S13, Supporting Information). The hemolysis ratio of all pollen cryogel groups consistently remained below 1.5%, much smaller than the minimal criteria of biomaterials hemocompatibility evaluation (5%) (Figure 6c). The hemocompatibility of the pollen cryogels was better than other demonstrated hemostats for deep noncompressible wound dressings.[14,59,63]

Apart from hemocompatibility, cytocompatibility represents another critical property for biomedical applications. The cytocompatibility of the pollen cryogels was evaluated through the cell viability measurement of mouse fibroblast cells (L929 cells, ATCC, USA) ($p < 0.05$) and human epidermal keratinocyte cells (HaCaT cells, CLS Cell Lines Service, Eppelheim, Germany) culturing in leaching solution collected from pollen cryogels. It was discovered that the viability index of mouse fibroblast cells (L929 cells) ($p < 0.05$) and human epidermal keratinocyte cells (HaCaT cells) was close to 95% and remained stable even after prolonged periods of cell culture, where pollen cryogels possessed good cytocompatibility (Figure 6d; Figure S14, Supporting Information). The cytocompatibility was further demonstrated by culturing the

L929 cells directly on pollen cryogels, and the cell viability was observed under a fluorescence microscope. There were always few dead cells on pollen cryogels within 3-day, and 7-day cell cultures, and even not obvious after cell culturing for 14 days (Figure 6e). Despite the autofluorescence properties of pollen, a significant amount of live cells were still visible on the macroporous structures of the cryogel (Figure 6e).

Finally, the hemostatic capacity of pollen cryogels was explored in a normal mouse liver injury wound model based on the total amount of blood loss and hemostatic time (**Figure 7a**).[14] This model was adopted since the composition of coagulation factors and regulatory proteins found in the blood plasma of mice are comparable to those in humans.[64] Without any absorbent, there was significant blood loss, and the blood spread fast on the large areas of filter papers. On the other hand, the wounds treated with pollen cryogels were observed to have the smallest bloodstain areas on the filter paper underneath the mouse livers, while much larger bloodstain areas were distributed on the filter papers when the wound was treated with cotton gauze, collagen sponge, CELOX gauze and CELOX grains (Figure 7b). The total amount of blood loss and the hemostatic time were also used to quantify the hemostatic effects of pollen cryogels and the other tested commercial products. Across all tested samples, pollen cryogels achieved the lowest amount of blood loss. Notably, pollen
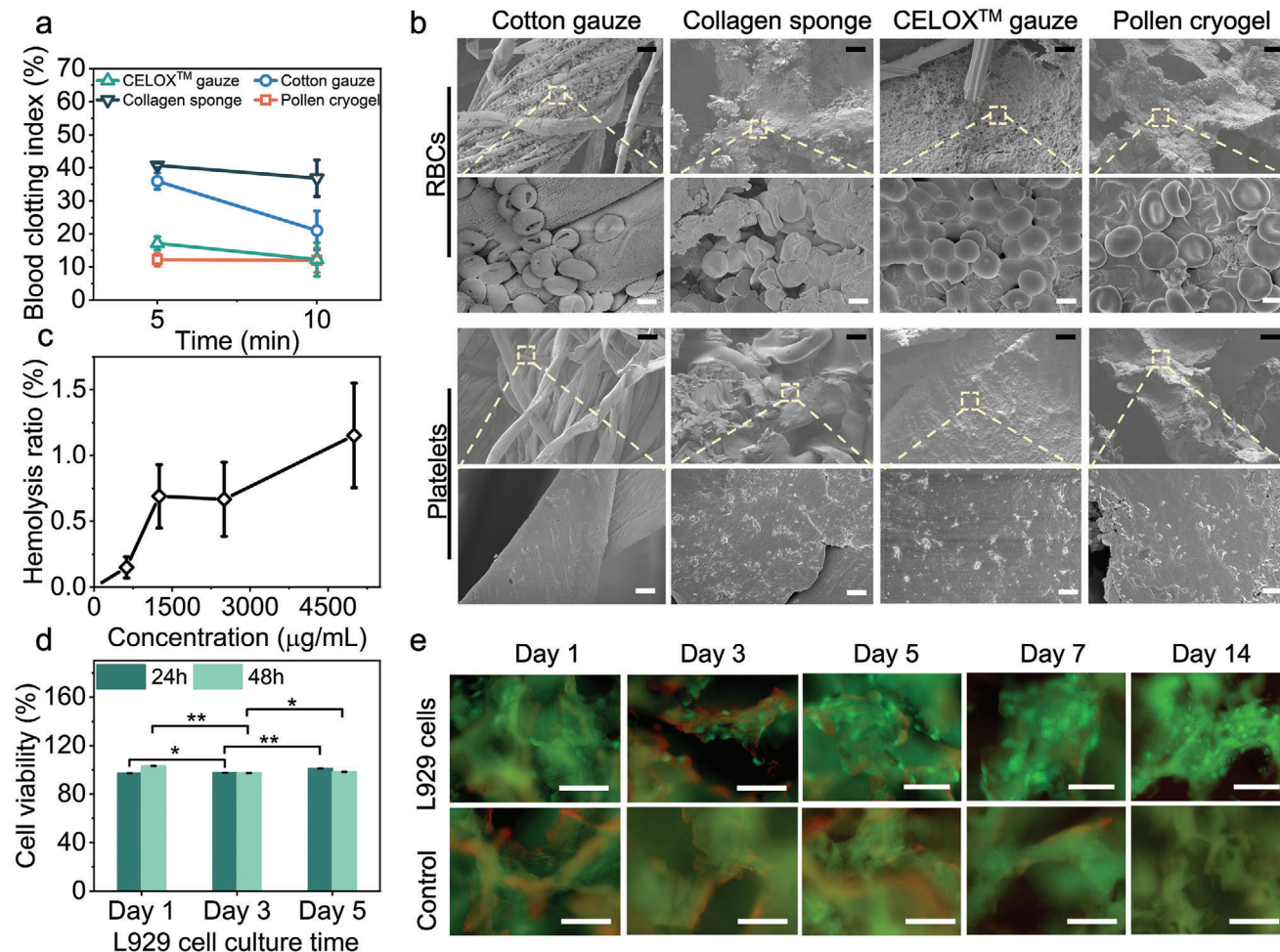
**ADVANCED
SCIENCE NEWS**

www.advancedsciencenews.com

**ADVANCED
MATERIALS**

www.advmat.de

Figure 6. Biological properties of the pollen cryogels: a) Comparison of blood clotting index values of pollen cryogels and other commercial products, namely cotton gauze, CELOX gauze, and collagen sponge. b) FESEM images with different magnifications of red blood cells (RBCs) and platelets adhesion on the pollen cryogels and other commercial products, namely cotton gauze, CELOX gauze, and collagen sponge. The black scale bars represent 20 µm, and the white scale bars represent 2 µm. c) Hemolytic ratio of the pollen cryogel dispersion liquids under different concentrations in PBS solution. d) Cytocompatibility evaluation of pollen cryogels with L929 cells across various cell culture times, including 1 day, 3 days, and 5 days. The 24 h and 48 h indicated the leaching content collecting time from pollen cryogels. e) Fluorescence microscope images of L929 cells cultured on pollen cryogels across 1, 3, 7, and 14 days. The white scale bars represent 50 µm. The statistical significance of the observed trends was calculated using Student's t-test (two-sided). $*p < 0.05$, $**p < 0.01$, $***p < 0.001$, $****p < 0.0001$, $n = 3$.

cryogels only demonstrated as low as 50% of blood loss of the best-performing commercial product, which is the collagen sponge ($p < 0.01$) (Figure 7c). With highly interconnected macroporous structures allowing blood to permeate into the interior rapidly, the pollen cryogels also demonstrated the shortest hemostatic time. The hemostatic time of the blank group without any absorbent (14.98 min) was the longest among all the groups ($p < 0.0001$). CELOX grains ($p < 0.0001$), cotton gauze ($p < 0.0001$), and CELOX gauze ($p < 0.01$) showed a hemostatic time of longer than 7 min, while the hemostatic time of pollen cryogels was the shortest at around 4.25 min, which is even shorter than collagen sponge (about 5.16 min) ($p < 0.001$) (Figure 7d).

To further investigate the potential for clinical translation of the pollen cryogel, we employed a lethal rabbit kidney injury model to assess their hemostatic efficacy in large animal settings (Figure S15, Supporting Information). Collagen sponge and cot-

ton gauze, commonly used for hemostasis in clinical scenarios, were used as comparators. Pollen cryogels demonstrated superior hemostatic performance. Only a small area of bloodstain was observed on the filter paper under the rabbit kidney treated with pollen cryogels, whereas large bloodstain areas were observed with the use of collagen sponges and cotton gauze (Figure S15b, Supporting Information). Pollen cryogels were easily compressed to fit the wound shape and rapidly recovered after absorbing blood, thereby filling the deep noncompressible wound and exerting pressure to stop bleeding within 2.72 ± 0.69 min (Figure S15c, Supporting Information). In contrast, untreated wounds continued bleeding for 7.49 ± 0.84 min, and collagen sponge and cotton gauze reduced hemostasis time to $\approx 4.69 \pm 1.17$ and 3.83 ± 0.26 min, respectively, which were not as efficient as pollen cryogels. Furthermore, statistical analysis revealed that pollen cryogels significantly reduced blood loss to only $\approx 0.38 \pm 0.07$ g, which
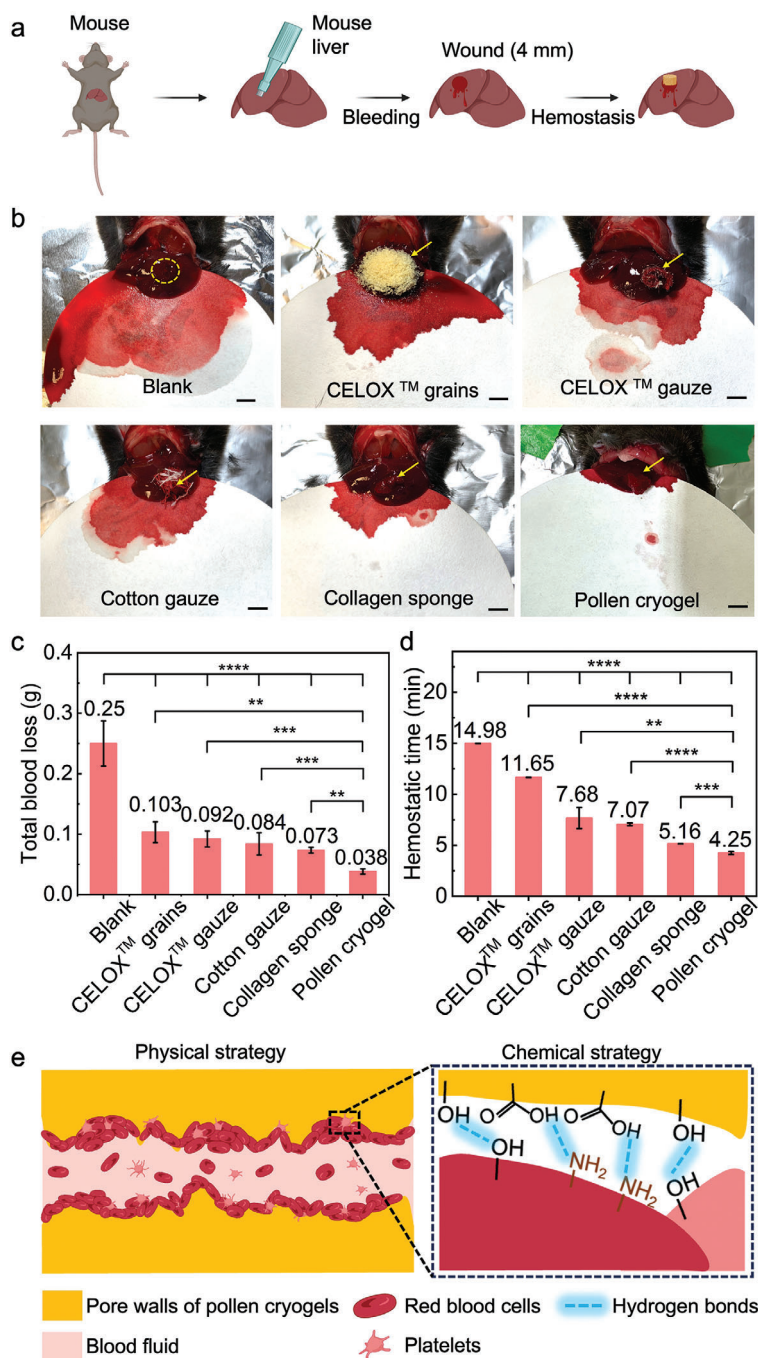
Figure 7. In vivo hemostatic capacity evaluation of the pollen cryogels in the normal mouse liver injury wound model: a) Schematic illustration of the experimental process of hemostasis in a mouse liver perforation wound model. b) Photographs of the hemostatic effect of the blank (without hemostat), CELOX grains, CELOX gauze, cotton gauze, collagen sponge, and pollen cryogels. The yellow arrow represents the bleeding site, and the yellow dotted circle represents the wound shape. The black scale bars represent 4 mm. Comparison of c) total blood loss and d) hemostatic time of pollen cryogels with blank (without hemostat) and other commercial products, including CELOX grains, CELOX gauze, cotton gauze, and collagen sponge. e) The hemostatic mechanism description of pollen cryogels: physical strategy (hierarchical high surface roughness) and chemical strategy (carboxyl groups and hydroxyl groups on the surface). The significant difference was detected using ANOVA and post hoc analysis (multigroup comparison), which was followed with T-tests: Two-sample assuming equal variance for pairwise comparison (alpha value: 0.05), then the Boferroni-adjustment was applied for post-hoc analysis. $*p < 0.05$, $**p < 0.01$, $***p < 0.001$, $****p < 0.0001$, $n = 3$.

**ADVANCED
SCIENCE NEWS**

www.advancedsciencenews.com

**ADVANCED
MATERIALS**

www.advmat.de

was much lower than the untreated groups (11.89 ± 2.46 g), collagen sponges (4.36 ± 2.60 g), and cotton gauze (2.3 ± 0.73 g) (Figure S15d, Supporting Information).

Hemostasis involves two main stages: the primary stage, which includes RBCs and platelets adherence and activation, and the secondary stage, which involves the coagulation cascade.[65] In the case of the pollen cryogels, the interconnected macroporous structures allowed rapid and substantial blood penetration, which enabled the cryogels to recover their shape, press the wound, and activate hemostasis. When blood perfused into the interior of our pollen cryogels, the spiky and bumpy surfaces with micro/nano hierarchical structures helped concentrate the blood cells, plasma proteins, and coagulation factors, facilitating rapid blood clotting.[60]

Additionally, the presence of numerous hydroxyl and carboxyl groups on the surfaces of pollen cryogels enables robust interactions with red blood cells and platelets. This interaction promotes the clustering of red blood cells and triggers platelet activation at the initial phase.[65] Moreover, the negatively charged carboxyl groups on the surface can interact with positively charged amino acids found in the coagulation factor XII chain.[65] This interaction initiates the intrinsic coagulation pathway, thus expediting the coagulation process in the subsequent phase. These combined physical and chemical mechanisms inherent to pollen cryogels significantly enhance their hemostatic efficacy in treating deep, noncompressible wounds, as demonstrated in Figure 7e.

Pollen cryogels, while offering several advantages,[39,46] come with the critical necessity of being surgically excised from wounds once hemostasis is achieved.[14,27,65] However, a redeeming feature is that these cryogels can be crafted with precision in both shape and dimension, ensuring an optimal fit to the wound. This better fit is instrumental in reducing injury during the removal procedure. Another benefit is the feasibility of mass production for these cryogels. They can be fabricated at scale by leveraging conventional soap-making processing methodologies.[39,46] Therefore, these features achieved that pollen cryogels can be used as first-aid rescue and prehospital hemostasis, especially for deep noncompressible wounds, before transferring patients for further special medical treatments.

Pollen cryogels present a more sustainable option compared to animal-derived alternatives like collagen sponges.[5,66] It's vital to underscore that unchecked animal farming has been a significant contributor to pressing environmental issues.[66] From a cost perspective, producing pollen cryogels is in the ballpark of the expenses associated with currently available commercial cellulose-based materials.[45]

3. Conclusion

In this work, we developed pollen-based cryogels as hemostats to treat noncompressible hemorrhage through compression-driven self-crosslinking of pollen microgel particles. The process is enabled by the close packing of granular structures and the hierarchical morphology of pollen microgel particles at both the micro- and nanoscale and eliminates the need for additional crosslinkers that may be harmful to human health. The pollen cryogels exhibited excellent mechanical strength and cyclic mechanical stability in a hydrated state, as well as good water and blood absorption ca-

pability with rapid water- and blood-triggered shape recovery. As hemostats, they performed better than other commercial products, including cotton gauze, collagen sponge, CELOX gauze, and CELOX grains, owing to inherent high surface roughness, as well as an abundance of carboxyl and hydroxyl groups on the surface of the pore walls, which facilitated the aggregation and adherence of RBCs and platelets. The hemostatic performance was further confirmed using a mouse liver perforation wound model, although further clinical trials are necessary to ascertain the human immune response to pollen cryogels during hemostasis. However, how pollen cryogels would promote wound healing remains a topic for further research.

Taken together, this work provides a sustainable design strategy for the fabrication of biosafe and non-allergenic pollen cryogels and points to their potential use in biomedical applications.

4. Experimental Section

Defatting of Sunflower Bee Pollens: 500 g of bee pollen was decanted in deionized water (1 L, 50 °C), mixed, and stirred for 2 h. The pollen suspension was passed through a nylon mesh (pore size: 200 μm in diameter) to remove sand and other contaminating particulate matter. The remaining pollen grains were collected by vacuum filtration and mixed with 1 L of acetone at room temperature. The mixture was stirred for 3 h (800 rpm) with an IKA disperser and filtered. The pollen was washed 3–4 times with fresh acetone again until the filtrate became clear. The filtered pollen powders were left in the fume hood overnight for 12 h to evaporate the acetone fully. Thereafter, the dried pollen powder was dispersed and stirred in diethyl ether (1 L) at room temperature for 2 h. This process was repeated twice more. The pollen was then mixed with fresh diethyl ether (1L) and stirred overnight to complete the reactions. Finally, the pollen powder was transferred into a glass petri dish and left in the fume hood to fully dry and recover the defatted pollen powder.

Pollen Microgel Preparation: Defatted pollen (20 g) was mixed with aqueous 10 wt% potassium hydroxide (KOH) (200 mL) solution and refluxed at 80 °C for 2 h with stirring at 800 rpm. The suspension was filtered using a nylon mesh (pore size: 30 μm in diameter) and the collected pollen samples were washed with fresh KOH solution (10 wt%) until the filtrate was clear. Following this, the samples were incubated in fresh KOH solution (10 wt%) at 80 °C for different incubation periods to undergo de-esterification, as previously reported.[39,43] Neutralization of the samples was then carried out with deionized (DI) water via the same nylon mesh (pore size: 35 μm), until the pH value reached around 7.5, resulting in the formation of pollen microgels. Then the pollen microgels with high water content were left in the oven (37 °C) for 24 h to decrease the water content.

Fabrication of Pollen Cryogels: The prepared pollen microgels were collected and pipetted into individual wells of a 24-well plate (2 mL per well). Freeze the plates in the refrigerator (at −20 °C) overnight. Then the plates containing the frozen microgels were immersed in ethanol (absolute for analysis EMSURE ACS) and thawed. The frozen microgel was allowed to stand in absolute ethanol for ≈48 h for thorough solvent exchange, resulting in ethanol-exchanged pollen microgels. Then the pollen samples were taken out and put in a petri dish to dry overnight at room temperature.

Calculation of Water Content in Pollen Microgel: The water content of pollen microgel was controlled by the evaporation time of pollen microgel suspensions in the ambient environment, which was measured by dropping a small amount of the suspension onto a weighing boat, weighing it (W_{gel}), then drying it in an oven and weighing it again (W_{dry}). The water content was calculated using the equation:

$$\text{Water content (\%)} = \left(W_{gel} - W_{dry} \right) / W_{gel} \times 100\% \tag{1}$$

Mechanical Properties of Pollen Cryogels: A dynamic mechanical analyzer was used (DMA Q800, TA instruments) in a controlled force mode.

**ADVANCED
SCIENCE NEWS**

www.advancedsciencenews.com

**ADVANCED
MATERIALS**

www.advmat.de

The pollen cryogels were held between parallel-plate compression clamps. To measure dry pollen cryogel samples, they were compressed at a 1 N min^{-1} ramp rate from 0.1 to 18.0 N. To characterize wet pollen cryogel samples, they were compressed at a 0.5 N min^{-1} ramp rate from 0.1 to 4.0 N. The compressive Young's modulus was calculated from the slope of the elastic region of the stress-strain curve, between 30% and 40% compressive strain. Cyclic compression recovery analysis of pollen cryogels was also conducted using the MTS Criterion Model 42 instrument (MTS Systems Corporation, USA) in a controlled strain mode. 50 cycles were performed on pollen cryogels with 1 mm min^{-1} compression up to the determined compressive strain and 0.01 mm min^{-1} decompression back to the original height. The cyclic compression tests were performed in the ambient environment at room temperature.

Characterization of Morphology of Macroporous Structure: The morphology of the macroporous structure was characterized using a field-emission scanning electron microscope (FESEM) (JSM-7600F Schottky field-emission scanning electron microscope). Samples were sputter-coated (JEOL) for 30 seconds under 40 kV before observation. To observe the sample structures during the self-crosslinking process, the dry pollen microgels, dry frozen microgels, and dry ethanol-immersed cryogels were prepared via freezing at −196 °C for 15 mins, followed by freeze-drying in a lyophilizer (Labcocon) for 48 h.

KBr-FTIR Spectrum Test: Fourier Transform infrared (FTIR) spectra of pollen samples(dry pollen microgels, freeze-dried frozen pollen microgels, freeze-dried ethanol-exchanged pollen microgels, and dry pollen cryogels) were measured with the PerkinElmer Spectrometer (PerkinElmer, UK) when mixed with potassium bromide (KBr) pellets. Reflectance IR spectra were obtained between 4000 and 600 cm^{-1} by means of 16 scanning per measurement. Background spectra were collected with pure KBr pellets prior to sample readings and subtracted from each sample spectrum automatically by Spectrum 10 Software (PerkinElmer, UK). To correct spectra with sloped baselines and reduce the amount of noise in the spectrum, a baseline correction and smoothing process was conducted after sample measurements using the software.

Swelling Ratio Test: Fully dried pollen cryogels at room temperature were firstly weighted (W_E). Then the pollen cryogels were immersed in DI water for around 15 min to absorb water thoroughly and weighed again (W_O). The swelling ratio (SR) was calculated according to the following equation:

$$SR = (W_E − W_O) /W_O × 100\% \tag{2}$$

The tests were repeatedly performed on pollen cryogels fabricated from microgel under different incubation time, 12, 24, 36, and 48 h.

Water and Blood Absorption Behavior: The volume of fully dried pollen cryogels (pollen cryogels from microgel incubated for different time, 12, 24, 36, and 48 h) was measured, called V (cm^3), then dry pollen cryogels contacted water. Hydrated pollen cryogels were compressed to squeeze out water, which were then weighed, called W_c (g). Afterward, the compressed pollen cryogels were immersed in DI water or anticoagulated whole blood (AWB) from mice. The blood was treated with the anticoagulants, EDTA (1 mL blood / 10 μL 10% EDTA solution). At various time spans, they were taken out to measure weight, which was called W_d (g). The water/blood absorption capacity was calculated as below:

$$\text{Water/Blood absorption capacity} \left(g\,cm^{-3} \right) = \frac{(Wd − Wc)}{V} \tag{3}$$

The water/blood absorption rate (g cm^{-3} s^{-1}) was calculated by analyzing the slope of the water/blood absorption capacity-time curve within 2 s.

To compare blood absorption behavior with commercial products, namely cotton gauze, CELOX-gauze, and collagen sponge, blood absorption capacity was also measured and calculated based on the equation above. Because commercial products were applied for hemostasis without hydrated preparation, they were weighted directly, as W_c (g).

Moreover, the blood absorption time was measured, and the behavior was further recorded using a digital camera. One drop of blood (500 μL) was pipetted on the pollen cryogels (24 h incubated) and each of the tested commercial products, respectively, and the absorption process was recorded using the digital camera. The absorption time off each sample was calculated based on the video playback.

Water- and Blood-Triggered Shape Memory Evaluation: The DI water content from hydrated pollen cryogels were squeezed out, before the cryogels were reimmersed in water and blood to recover its shape. The compressed and shape-fixed cryogels were soaked in water and blood while the process was recorded using a digital camera. The shape recovery ratio was characterized depending on height changes before and after re-absorbing water andblood. The shape recovery time was calculated based on the video playback. Additionally, the morphology of compressed and recovered macrostructures was further observed by FESEM.

Blood Clotting Index Test: The procoagulant ability of the pollen cryogels was evaluated by measuring the blood clotting index (BCI). Cotton gauze, collagen sponge, and CELOX gauze were used as controls. The pollen cryogels were compressed to squeeze out water and placed in EP tubes. After warming for 10 min at 37 °C, 50 μL of the anticoagulated whole blood (AWB) from rats was dropped onto their top surfaces. After incubation for 5 and 10 min at 37 °C, 3 mL of deionized water was added into each EP tube, and the optical density value at 540 nm (OD$_{540\,nm}$) of the supernatant was determined using a microplate reader and called OD$_{hemostat}$. The mixed DI water/AWB (3 mL/50 μL) solution was used as a negative control, and its OD$_{540\,nm}$ value was used as a reference value (OD$_{reference\,value}$). The BCI was calculated based on the following equation:

$$BCI (\%) = OD_{hemostat}/OD_{reference\,value} × 100\% \tag{4}$$

Hemocompatibility Evaluation: For hemolytic activity assay, the erythrocytes were obtained by centrifuging (at 400 × g) the mouse blood for 10 min. PBS was used to wash the obtained erythrocytes three times, and then the purified erythrocytes were diluted to a final concentration of 5% (v/v). After that, the dried pollen cryogel samples were smashed into homogenate by employing a tissue grinder, and four sample dispersion liquids (with the concentrations varying from 5 to 2.5, 1.25, and 0.625 mg mL^{-1}) were prepared. 0.5 mL of the pollen cryogel dispersion liquid and 500 μL of erythrocyte suspension (5% (v/v)) were added into a 2-mL tube and then gently mixed by pipetting. After being placed at 37 °C for 1 h, all the samples were centrifuged at 116 × g for 10 min. A volume of 500 μL of the supernatants was carefully transferred into new tubes, respectively. Then the supernatants were further centrifuged at 11 617× g for 10 min allowing exhaustively removal of the cryogel particles. The obtained supernatants were transferred into a new 96-well clear plate. The absorbance of the solutions at 540 nm was read using a microplate reader (Molecular Devices). 0.1% Triton X-100 served as the positive control and PBS served as the negative control.

The hemolysis percentage of the pollen cryogel was calculated using the equation:

$$\text{Hemolysis} (\%) = \left[(A_p − A_b) / (A_t − A_b) \right] × 100\% \tag{5}$$

where A_p was the absorbance value of supernatant from the cryogel groups, A_t was the absorbance value of the Triton X-100 positive control, and A_b was the absorbance value of PBS. Each group contains three repeats.

RBC and Platelet Adhesion Assays: The blood cell and platelet adhesion assay were performed according to reference.[14,59] The pollen sample was cut into disks with a height of 5 mm and a diameter of 8 mm, which were further immersed into PBS for 1 h at 37 °C, followed by squeezing out the PBS. After that, the anticoagulated whole blood (AWB) was dropwise introduced onto the pollen disks and then placed at 37 °C for 5 min. Platelet-rich plasma (PRP) was obtained by centrifuging the AWB (116x g) for 10 min at 4 °C. Then, PRP was dropwise introduced onto the pollen disks and further placed at 37 °C for 1 h. At the end of the time, all the test samples were washed with PBS three times to remove the physically adhered blood cell and platelet. Then the samples were fixed using a 2.5% glutaraldehyde for another 2 h. After that, blood cells and platelets in the samples were gradually dehydrated using 50%, 60%, 70%, 80%, 90%, and 100% ethanol

solution with a time interval of 10 min. The dried samples were observed using FESEM.

Cytocompatibility Evaluation: The cytocompatibility was characterized by the LIVE/DEAD Viability/Cytotoxicity Kit (Invitrogen) and Cell counting kit (CCK-8, Dojindo Laboratories) with L929 cells and HaCaT cells. The cells were cultured in a humidified 5% CO_2 incubator at 37 °C, which the Dulbecco's modified eagle medium (DMEM) (Gibco) supplemented with 10% fetal bovine serum (Gibco), and 1% penicillin-streptomycin (Hyclone) was used as the complete growth medium.

To evaluate the cell viability index of releases from the cryogels, the pollen cryogels were immersed in the medium (1 dry pollen cryogel/ 10 mL of DMEM). The medium was collected as the leaching solution after 24 and 48 h immersion. The cells were seeded in a 96-well plate (5×10^3 cells/ well), and the medium was replaced by 24- and 48-h leaching solutions. The cell viability was determined after 1, 3, and 5 days by using leaching solutions of pollen cryogels. The CCK-8 agent was added and further incubated for 2 h, and the cell viability was determined by absorbance at 450 nm using the microplate reader.

For the fluorescence live/dead assay, the dry pollen cryogels were cut into square layers with 5 mm of width and 1 mm of thickness and sterilized to remove any contamination under UV light for around 30 min. Then, the dry pollen cryogels were immersed in a culture medium to swell enough and squeezed out, which cryogels were placed into each well in a 48-well plate. Then, L929 cell suspensions were dropped on the surface of the scaffolds (2×10^4 cells/well) and incubated to allow attachment cells to the pollen cryogels. Live/Dead assay was implemented (Calcein-AM for green live cells or ethidium homodimer-1 for red dead cells) after incubation after 1, 3, 5, 7, and 14 days, and each group was repeated twice. The cells were then observed using a Zeiss fluorescence microscope (Axio Observer Z1, Carl Zeiss, Oberkochen, Germany).

Hemostasis in Vivo: All procedures involving mice were conducted following the guidelines set by the Biomedical Sciences Institute's Institutional Animal Care Committee (IACUC #211 636) and in accordance with the standards established by the Biological Resource Centre, Agency of Science, Technology, and Research (A*STAR), Singapore. Mice were kept with their littermates (2–5 in each cage) in individual ventilation cages, maintained on a 12-hour light/dark rotation. Throughout the study, they had unrestricted access to water and were fed with Altromin 1324 irradiated modified food containing 18% Protein and 6% Fat. The in vivo hemostasis capability of pollen cryogels was evaluated alongside no-treatment (negative control) and commercially available materials (cotton gauze, collagen sponge, CELOX gauze, and CELOX grains) with the mouse liver trauma model. The pollen cryogel is softened with PBS solution and compressed on a piece of tissue to remove the PBS solution before use. C57BL/6 mice under 4 to 5 weeks – old of mixed genders were used, and each group contained five mice. The animals were anesthetized with 150 mg k^{-1}g ketamine and 10 mg k^{-1}g xylazine administered intraperitoneally. The mouse liver was exposed by an abdominal incision, and serous fluid around the mouse liver was carefully removed to prevent inaccuracies in the estimation of the blood weight obtained by the hemostatic samples. The mouse liver was lifted and placed onto the surface of a pre-weighted filter paper. A circular surface defect (diameter of 4 mm) was created on the mouse liver to induce hemorrhaging through a biopsy punch. The hemostatic agents were immediately applied onto the defect with slight pressure and left on the surface defect for 15 min. The total blood loss is obtained from the subtraction of the original from the final filter paper weight, while the hemostatic time refers to the time required.

All procedures involving rabbits were conducted following the guidelines set by the Biomedical Sciences Institute's Institutional Animal Care Committee (IACUC #240 068). 8-week-old (2–2.5 kg) rabbits are used in this experiment. Rabbits will be put to sleep with the induction at 4–5% and maintenance at 2–3% isoflurane in the air using a face mask. The rabbit's abdomen was shaved, and a midline laparotomy was performed to expose the viscera. Serous fluid around the kidney and the tissues around the kidney were carefully removed to prevent inaccuracies in the estimation of the blood weight obtained by hemostatic samples. The kidney was lifted and placed on the surface of pre-weighted filter papers. A circular deep wound (diameter of 8 mm) was made on the rabbit kidney to in-

duce hemorrhaging through a biopsy punch. Different hemostatic agents are immediately put into each kidney, applied onto the wound with slight pressure, and left on the surface defect for 15 min. The total blood loss is obtained from the subtraction of the original from the final filter paper weight, while the homeostatic time refers to the time required. The digital photos were taken after 15 mins.

Statistical Analysis:

1) This manuscript did not contain the data with transformation or normalizations.
2) The data presentation in the description for Figure 4f: mean ± SD.
3) Sample size, $n = 3$, average value calculation and standard deviation calculation were based on the function in the software, Microsoft Excel: Average and STDEV. P.
4) The statistical method to assess the significance difference, P value, in Figures 4e,f and 6d, used the Student's t-test when only two groups were compared. The statistical method to assess the significant difference, P value, in Figure 7c,d (Multigroup comparison), used one-way ANOVA & post hoc analysis when comparing multigroup samples, which was followed with t-tests: Two-sample assuming equal variance for pairwise comparison (Alpha value: 0.05), then the Bonferroni-adjustment was applied for post hoc analysis. *$p < 0.05$, **$p < 0.01$, ***$p < 0.001$, ****$p < 0.0001$, $n = 3$.
5) Statistical analysis software: Microsoft Excel.

Supporting Information

Supporting Information is available from the Wiley Online Library or from the author.

Conflict of Interest

The authors declare no conflict of interest.

Data Availability Statement

Research data are not shared.

[1] B. Gegel, J. Burgert, J. Gasko, C. Campbell, M. Martens, J. Keck, H. Reynolds, M. Loughren, D. Johnson, *Mil. Med.* **2012**, *177*, 1543.

ADVANCED
SCIENCE NEWS

www.advancedsciencenews.com

ADVANCED
MATERIALS

www.advmat.de

[2] J. B. Holcomb, *Crit. Care* **2004**, *8*, S57.

[3] N. Vilardo, J. Feinberg, J. Black, E. Ratner, *Gynecol. Oncol. Rep.* **2017**, *21*, 114.

[4] Y. Huang, X. Zhao, Z. Zhang, Y. Liang, Z. Yin, B. Chen, L. Bai, Y. Han, B. Guo, *Chem. Mater.* **2020**, *32*, 6595.

[5] S. Lv, M. Cai, F. Leng, X. Jiang, *Carbohydr. Polym.* **2022**, *288*, 119369.

[6] S. W. Rothwell, J. M. Fudge, W. K. Chen, T. J. Reid, C. Krishnamurti, *Thromb. Res.* **2002**, *108*, 335.

[7] T. L. Landsman, T. Touchet, S. M. Hasan, C. Smith, B. Russell, J. Rivera, D. J. Maitland, E. Cosgriff-Hernandez, *Acta Biomater.* **2017**, *47*, 91.

[8] X. Yang, W. Liu, Y. Shi, G. Xi, M. Wang, B. Liang, Y. Feng, Y. Ren, C. Shi, *Acta Biomater.* **2019**, *99*, 220.

[9] G. R. Mueller, T. J. Pineda, H. X. Xie, J. S. Teach, A. D. Barofsky, J. R. Schmid, K. W. Gregory, *J. Trauma Acute Care Surg.* **2012**, *73*, S134.

[10] M. B. B. Monroe, A. D. Easley, K. Grant, G. K. Fletcher, C. Boyer, D. J. Maitland, *ChemPhysChem* **2018**, *19*, 1999.

[11] Y. J. Yu, K. Hearon, T. S. Wilson, D. J. Maitland, *Smart Mater. Struct.* **2011**, *20*, 085010.

[12] G. Ellson, M. D. Prima, T. Ware, X. Tang, W. Voit, *Smart Mater. Struct.* **2015**, *24*, 055001.

[13] A. U. Vakil, N. M. Petryk, E. Shepherd, M. B. B. Monroe, *Polymers* **2021**, *13*, 4084.

[14] X. Zhao, B. Guo, H. Wu, Y. Liang, P. X. Ma, *Nat. Commun.* **2018**, *9*, 2784.

[15] V. M. Gun'ko, I. N. Savina, S. V. Mikhalovsky, *Adv. Colloid Interface Sci.* **2013**, *187*, 1.

[16] A. Memic, T. Colombani, L. J. Eggermont, M. Rezaeeyazdi, J. Steingold, Z. J. Rogers, K. J. Navare, H. S. Mohammed, S. A. Bencherif, *Adv. Therap.* **2019**, *2*, 1800114.

[17] L. Qian, H. Zhang, *J. Chem. Technol. Biotechnol.* **2011**, *86*, 172.

[18] K. Rybak, O. Parniakov, K. Samborska, A. Wiktor, D. Witrowa-Rajchert, M. Nowacka, *Sustainability* **2021**, *13*, 2035.

[19] Y. Saylan, A. Denizli, *Gels* **2019**, *5*, 20.

[20] R. Maciulaitis, J. L. Robert, B. S. Lima, S. Ruiz, *Nat. Rev. Drug Discov.* **2010**, *9*, 195.

[21] A. Molero, M. Calabro, M. Vignes, B. Gouget, D. Gruson, *Ann. Lab. Med.* **2021**, *41*, 139.

[22] K. Kraiwattanawong, N. Sano, H. Tamon, *Carbon* **2011**, *49*, 3404.

[23] T. Widmann, L. P. Kreuzer, N. Hohn, L. Biessmann, K. Wang, S. Rinner, J. F. Moulin, A. J. Schmid, Y. Hannappel, O. Wrede, M. Kuhnhammer, T. Hellweg, R. von Klitzing, P. Muller-Buschbaum, *Langmuir* **2019**, *35*, 16341.

[24] Y. Ni, X. Zhou, J. Gong, L. Xue, Q. Zhao, *Adv. Funct. Mater.* **2021**, *31*, 2103818.

[25] J. Erlandsson, H. Francon, A. Marais, H. Granberg, L. Wagberg, *Biomacromolecules* **2019**, *20*, 728.

[26] L. Zheng, Q. Wang, Y. S. Zhang, H. Zhang, Y. Tang, Y. Zhang, W. Zhang, X. Zhang, *Chem. Eng. J.* **2021**, *416*, 129136.

[27] X. Fan, Y. Li, X. Li, Y. Wu, K. Tang, J. Liu, X. Zheng, G. Wan, *Int. J. Biol. Macromol.* **2020**, *154*, 1185.

[28] J. Erlandsson, T. Pettersson, T. Ingverud, H. Granberg, P. A. Larsson, M. Malkoch, L. Wågberg, *J. Mater. Chem. A* **2018**, *6*, 19371.

[29] G. Lan, B. Lu, T. Wang, L. Wang, J. Chen, K. Yu, J. Liu, F. Dai, D. Wu, *Colloids Surf., B: Biointerfaces* **2015**, *136*, 1026.

[30] M. Li, Z. Zhang, Y. Liang, J. He, B. Guo, *ACS Appl. Mater. Interfaces* **2020**, *12*, 35856.

[31] Z. Zhao, J. Kumar, Y. Hwang, J. Deng, M. S. Ibrahim, C. Huang, S. Suresh, N. J. Cho, *Proc. Natl. Acad. Sci. USA* **2021**, *118*, 2113715118.

[32] S. M. Andrabi, P. Singh, S. Majumder, A. Kumar, *Chem. Eng. J.* **2021**, *423*, 130219.

[33] Z. Huang, H. Zhang, M. Guo, M. Zhao, Y. Liu, D. Zhang, M. Terrones, Y. Wang, *Carbon* **2022**, *194*, 23.

[34] X. Zhao, Y. Liang, B. Guo, Z. Yin, D. Zhu, Y. Han, *Chem. Eng. J.* **2021**, *403*, 126329.

[35] Y. Huang, X. Zhao, C. Wang, J. Chen, Y. Liang, Z. Li, Y. Han, B. Guo, *Chem. Eng. J.* **2022**, *427*, 131977.

[36] M. Jaishankar, T. Tseten, N. Anbalagan, B. B. Mathew, K. N. Beeregowda, *Interdiscip. Toxicol.* **2014**, *7*, 60.

[37] G. S. Simate, S. E. Iyuke, S. Ndlovu, M. Heydenrych, L. F. Walubita, *Environ. Int.* **2012**, *39*, 38.

[38] R. C. Mundargi, M. G. Potroz, S. Park, H. Shirahama, J. H. Lee, J. Seo, N. J. Cho, *Small* **2016**, *12*, 1167.

[39] T. F. Fan, S. Park, Q. Shi, X. Zhang, Q. Liu, Y. Song, H. Chin, M. S. B. Ibrahim, N. Mokrzecka, Y. Yang, H. Li, J. Song, S. Suresh, N. J. Cho, *Nat. Commun.* **2020**, *11*, 1449.

[40] W. Wang, G. Yang, H. Cui, J. Meng, S. Wang, L. Jiang, *Adv. Healthcare Mater.* **2017**, *6*, 1700003.

[41] R. C. Mundargi, M. G. Potroz, J. H. Park, J. Seo, J. H. Lee, N.-J. Cho, *RSC Adv.* **2016**, *6*, 16533.

[42] T. Zhao, T. Yuan, T. Li, L. Chen, X. Li, J. Zhang, *ACS Appl. Mater. Interfaces* **2020**, *12*, 55362.

[43] T. F. Fan, Y. Hwang, M. S. Ibrahim, G. Ferracci, N. J. Cho, *Macromol. Rapid Commun.* **2020**, *41*, 2000155.

[44] Z. Zhao, Y. Hwang, Y. Yang, T. Fan, J. Song, S. Suresh, N. J. Cho, *Proc. Natl. Acad. Sci. USA* **2020**, *117*, 8711.

[45] Z. Zhao, J. Deng, H. Tae, M. S. Ibrahim, S. Suresh, N. J. Cho, *Adv. Mater.* **2022**, *34*, 2109367.

[46] Y. Hwang, M. S. B. Ibrahim, J. Deng, J. A. Jackman, N. J. Cho, *Adv. Funct. Mater.* **2021**, *31*, 2101091.

[47] T. Baran, I. Sargin, M. Kaya, A. Mentes, T. Ceter, *J. Colloid Interface Sci.* **2017**, *486*, 194.

[48] T.-F. Fan, Y. Hwang, M. G. Potroz, K.-L. Lau, E.-L. Tan, M. Shahrudin Ibrahim, E. Miyako, N.-J. Cho, *Appl. Mater. Today* **2020**, *19*, 100594.

[49] T. F. Fan, M. G. Potroz, E. L. Tan, J. H. Park, E. Miyako, N. J. Cho, *Sci. Rep.* **2019**, *9*, 2944.

[50] T. F. Fan, M. G. Potroz, E. L. Tan, M. S. Ibrahim, E. Miyako, N. J. Cho, *Sci. Rep.* **2019**, *9*, 9626.

[51] F. Xu, J. Yu, T. Tesso, F. Dowell, D. Wang, *Appl. Energy* **2013**, *104*, 801.

[52] J. Grdadolnik, F. Merzel, F. Avbelj, *Proc. Natl. Acad. Sci. USA* **2017**, *114*, 322.

[53] J. Joseph, E. D. Jemmis, *J. Am. Chem. Soc.* **2007**, *129*, 4620.

[54] R. Gautam, N. Kumar, J. G. Lynam, *J. Mol. Struct.* **2020**, *1222*, 128849.

[55] I. Bouhid de Aguiar, K. Schroën, M. Meireles, A. Bouchoux, *Colloids Surf. A* **2018**, *553*, 406.

[56] Q. Shi, M. S. B. Ibrahim, X. Zhang, Y. Hwang, H. Chin, S. Chen, W. S. Tan, H. Li, J. Song, N.-J. Cho, *Appl. Mater. Today* **2022**, *27*, 101471.

[57] Y. Li, N. Grishkewich, L. Liu, C. Wang, K. C. Tam, S. Liu, Z. Mao, X. Sui, *Chem. Eng. J.* **2019**, *366*, 531.

[58] H. Françon, Z. Wang, A. Marais, K. Mystek, A. Piper, H. Granberg, A. Malti, P. Gatenholm, P. A. Larsson, L. Wågberg, *Adv. Funct. Mater.* **2020**, *30*, 1909383.

[59] X. Du, L. Wu, H. Yan, Z. Jiang, S. Li, W. Li, Y. Bai, H. Wang, Z. Cheng, D. Kong, L. Wang, M. Zhu, *Nat. Commun.* **2021**, *12*, 4733.

[60] S. S. Biranje, J. Sun, Y. Shi, S. Yu, H. Jiao, M. Zhang, Q. Wang, J. Wang, J. Liu, *Cellulose* **2021**, *28*, 8899.

[61] G. Li, K. Quan, Y. Liang, T. Li, Q. Yuan, L. Tao, Q. Xie, X. Wang, *ACS Appl. Mater. Interfaces* **2016**, *8*, 35071.

[62] A. Sasidharan, L. S. Panchakarla, A. R. Sadanandan, A. Ashokan, P. Chandran, C. M. Girish, D. Menon, S. V. Nair, C. N. Rao, M. Koyakutty, *Small* **2012**, *8*, 1251.

[63] L. Yao, H. Gao, Z. Lin, Q. Dai, S. Zhu, S. Li, C. Liu, Q. Feng, Q. Li, G. Wang, X. Chen, X. Cao, *Chem. Eng. J.* **2022**, *428*, 131005.

[64] B. M. Mohammed, D. M. Monroe, D. Gailani, *Platelets* **2020**, *31*, 417.

[65] H. Montazerian, E. Davoodi, A. Baidya, S. Baghdasarian, E. Sarikhani, C. E. Meyer, R. Haghniaz, M. Badv, N. Annabi, A. Khademhosseini, P. S. Weiss, *Chem. Rev.* **2022**, *122*, 12864.

[66] C. J. Bryant, *Future Foods* **2022**, *6*, 100174.